**Oceanic redox conditions through the late Pliensbachian to early Toarcian on the northwestern Panthalassa margin: Insights from pyrite and geochemical data**

Kentaro Izumi[a*], Kasumi Endo[b], David B. Kemp[c], Mutsuko Inui[b]

[a] *Faculty & Graduate School of Education, Chiba University, 1-33 Yayoi-cho, Inage-ku, Chiba-shi, Chiba 263-8522, Japan*

[b] *School of Science and Engineering, Kokushikan University, 4-28-1 Setagaya, Setagaya-ku, Tokyo 154-8515, Japan*

[c] *School of Geosciences, University of Aberdeen, Old Aberdeen, Aberdeen, AB24 3UE, UK*

*E-mail: izumi@chiba-u.jp (corresponding author)

## Abstract

The early Toarcian oceanic anoxic event (T-OAE; ~183 Ma) was a significant palaeoenvironmental perturbation associated with marked changes in oceanic redox conditions. However, the precise redox conditions and redox history of various water masses during the T-OAE, especially those from outside the Boreal and Tethyan realms, are unclear. To address this issue, we present pyrite framboid data from an upper Pliensbachian to lower Toarcian succession deposited on the NW Panthalassic margin in a shallow-water setting (Sakuraguchi-dani section, Toyora area, SW Japan).

Available data on redox-sensitive trace elements from the same succession suggest that dysoxic bottom-water conditions generally prevailed, with intermittent short-term oxygenation events. Size-distribution analysis of pyrite framboids reveals that framboid size populations from the silty mudstones during the OAE were characterized by small mean diameters and standard deviations. This suggests that euxinic conditions at least intermittently occurred during the T-OAE interval. Most likely, this water-column euxinia was associated with the expansion of an oxygen minimum zone linked to increased primary productivity. This interpretation is consistent with a previously reported increase in fluvial discharge and thus nutrient flux caused by a strengthening of the hydrological cycle.

Keywords: euxinia; pyrite framboid; trace element; vanadium; Toyora Group; Japan

## 1. Introduction

The early Toarcian oceanic anoxic event (T-OAE; ~183 Ma) represents one of the most significant paleoenvironmental perturbations of the Mesozoic, resulting in marked disruption to both the climate system and biosphere. The T-OAE was associated in particular with the widespread, ostensibly global, deposition of organic-rich facies under generally reducing conditions (Jenkyns, 1988; Fig. 1A). These strata are characterized by a marked negative excursion of ~3-7 ‰ in carbon isotopes ($\delta^{13}C$) of marine organic matter, marine carbonate and terrestrial plant material from open- to marginal-marine settings (e.g. Hesselbo et al., 2000; Jenkyns et al., 2001; Al-Suwaidi et al., 2010; Caruthers et al., 2011; Gröcke et al., 2011; Kafousia et al., 2011; Izumi et al., 2012). Studies of compound specific carbon isotopes suggest that the absolute magnitude of the $\delta^{13}C$ negative excursion was ~3-4 ‰ (Schouten et al., 2000; French et al., 2014; see also Suan et al., 2015). This feature has been attributed to a large-scale transfer of carbon-12 through the exogenic carbon cycle, possibly from methane hydrate dissociation or from carbon released thermogenically from organic matter sources. The ultimate trigger for both these carbon sources may have been the Karoo-Ferrar Large Igneous Province (Hesselbo et al., 2000; Kemp et al., 2005; McElwain et al., 2005; Svensen et al., 2007).

Coeval with the negative $\delta^{13}C$ excursion in a number of locations is associated evidence for abrupt seawater warming, ocean acidification, enhanced hydrological cycling, an increase in continental weathering rates, and ocean deoxygenation (Bailey et al., 2003; Pearce et al., 2008; Dera et al., 2009; Trecalli et al., 2012; Kemp and Izumi, 2014; Brazier et al., 2015; Krencker et al., 2015; Fujisaki et al., 2016; Percival et al., 2016). In addition, marine organisms were negatively affected by oxygen-depleted conditions during the T-OAE, resulting in mass extinction, elevated rates of biotic turnover, and organism size reduction (e.g. Morten and Twitchett, 2009; Caswell and Coe, 2013; Danise et al., 2013). Previous studies have suggested that euxinic conditions existed during the T-OAE in Boreal/Tethyan shallow-marine and Panthalassic pelagic settings, based on the geochemistry of redox-sensitive elements, biomarker evidence, and framboidal pyrite data (e.g. Schouten et al., 2000; Bowden et al., 2006; van Breugel et al., 2006; Wignall et al., 2010; Fujisaki et al., 2016). However, in shallow-water settings of Panthalassa the precise redox conditions (e.g. euxinic/anoxic, suboxic, dysoxic, oxic; Tyson and Pearson, 1991) and deoxygenation history through the T-OAE are unclear.

To address this issue, a new petrographic investigation of pyrite framboid size, coupled with new carbon-isotope analyses, has been carried out on strata deposited on the northwestern margin of the Panthalassa Ocean, and which is now exposed in southwestern Japan. This section, deposited on a shallow-marine setting, has recently been shown to preserve a record of the early Toarcian negative $\delta^{13}C$ excursion spanning ~35 m (Izumi et al., 2012; Kemp and Izumi, 2014). As such, the $\delta^{13}C$ excursion of the T-OAE is one of the most expanded yet described, and thus ideally suited to assess the relationship between the T-OAE carbon-cycle perturbation and redox changes.

Quantification of the size distribution of pyrite framboids is an established redox proxy, and this method has been used for reconstructing the palaeo-redox history of a number of geological intervals such as the Latest Permian to Triassic (e.g. Huang et al., 2017; Liao et al., 2017). Therefore, framboid data of the present study hold potential for better understanding the nature of redox changes through the T-OAE in the shallow Panthalassa margin setting. Pyrite framboids are an established indicator of redox conditions in both modern and ancient basins, and in a variety of settings such as lagoon, shelf, and offshore deep-water environments (e.g. Schallreuter, 1984; Lallier-Verges et al., 1993; Wilkin et al., 1996; Wilkin and Arthur, 2001; Neumann et al., 2005; Brunner et al., 2006; Wignall et al., 2010; Li et al., 2016). Importantly, the framboid redox indicator is also considered to be generally robust to diagenetic effects, and likely less affected by diagenesis compared with geochemical redox proxies (Wilkin et al., 1997).

In marine environments, the formation of pyrite framboids occurs in sediments or the water column immediately subjacent to the redox interface separating $O_2$-bearing and sulphide-bearing waters. When euxinia occurs in marine environments, pyrite framboids are formed in the water column, and quickly sink to the seafloor inhibiting growth to large size (e.g. Li et al., 2016). On the other hand, in normal marine sediments in oxygenated waters, the redox interface is located just below the sediment-water interface. Here, a relatively longer growth time allows larger pyrite framboids to develop (Wilkin et al., 1996). Based on numerous previous studies, a relationship between the size distribution of pyrite framboids (mean and standard deviation) and marine redox conditions has been established (Table 1). Euxinic conditions are characterized by small-sized framboids (mean diameter < ~5 μm) and relatively narrow size ranges, with rare pyrite crystals and amorphous lumps (Wilkin et al., 1996; Wignall et al., 2010; Table 1). Oxic to dysoxic conditions are characterized by larger sizes (mean diameter = 6 to 13 μm) and a wider size range (Wilkin et al., 1996; Wignall and Newton, 1998; Brunner et al., 2006; Wignall et al., 2010; Table 1). Although it is difficult to clearly distinguish between euxinic and suboxic-anoxic conditions (cf. Wignall et al., 2010), suboxic to anoxic conditions may be characterized by relatively small-sizes (mean diameter = ~5 to 6 μm) with more common presence of pyrite crystals and amorphous lumps (Wilkin et al., 1996; Wignall and Newton, 1998; Wignall et al., 2010; Table 1).

## 2. Geological setting and international correlation

Lower Jurassic siliciclastic sedimentary rocks of the Toyora Group crop out in the Toyora area of Yamaguchi prefecture, southwestern Japan (Fig. 1). The Nishinakayama Formation (middle part of the Toyora Group) consists mainly of Pliensbachian-Toarcian shallow-marine (below at least fair weather wave base) silty mudstones and sandstones (Tanabe, 1982; Kawamura, 2010; Nakada and Matsuoka, 2011). Lithofacies of mudstones from the Nishinakayama Formation are generally laminated, although bioturbated/burrowed mudstones are also frequently recognized

(Izumi et al., 2012; Fig. 2). In the Sakuraguchi-dani succession of the Toyora area (34° 08'N 131° 03'E; Fig. 1), the Nishinakayama Formation is exposed in mountainside ephemeral streambeds. This succession is bio- and chemo-stratigraphically well constrained by previous studies (Hirano, 1973; Tanabe, 1991; Nakada and Matsuoka, 2011; Izumi et al., 2012; Kemp and Izumi, 2014).

High-resolution $\delta^{13}C$ analysis of organic matter ($\delta^{13}C_{org}$) through the succession has revealed a ~3.5 ‰ negative excursion spanning ~35 m (Kemp and Izumi, 2014; Izumi et al., 2018). This record is unambiguously interpreted as the T-OAE based on the structure of the excursion and age constraints provided by a detailed ammonite biostratigraphy correlable to northern Europe (Izumi et al., 2012; Kemp and Izumi, 2014; Izumi et al., 2018). The biostratigraphic framework for the Sakuraguchi-dani succession is well established (e.g. Hirano, 1973). The latest refinements of Nakada and Matsuoka (2011) have delineated three key ammonite zones within the Nishinakayama Formation of the Sakuraguchi-dani succession: the *Palparites paltus* Zone, the *Dactylioceras helianthoides* Zone, and the *Harpoceras inouyei* Zone (Nakada and Matsuoka, 2011; Fig. 2). Nakada and Matsuoka (2011) and Izumi et al. (2012) established a correlation between this Japanese zonation and the northern European zonation (e.g. Page, 2003). This put the base of the *P. paltus* Zone at the Pliensbachian-Toarcian boundary (i.e. base *Dactylioceras tenuicostatum* Zone in northern Europe). *D. helianthoides* has been recovered from the upper part of the *tenuicostatum* Zone of northern Europe, as well as the *tenuicostatum* Subzone of a southwestern Panthalassa section exposed in Chile (Schmidt-Effing, 1972; Von Hillebrandt and Schmidt-Effing, 1981). These observations are consistent with knowledge of the position of the onset of the $\delta^{13}C_{org}$ excursion in Japan and Europe, which is close to the first occurrence of *D. helianthoides* in the Sakuraguchi-dani section, and occurs in the upper part of the *tenuicostatum* Zone of Yorkshire, UK (see Fig. 2 of Kemp and Izumi, 2014).

## 3. Materials and methods

### *3.1. Carbon isotopes and TOC analysis*

A total of 11 silty mudstone samples were collected from a newly recognised outcrop stratigraphically below the strata previously studied by both Izumi et al. (2012) and Kemp and Izumi (2014). The age is likely to be late Pliensbachian based on the work of Nakada and Matsuoka (2011) (Fig. 3). According to Nakada and Matsuoka (2011), the stratigraphic position of the Pliensbachian-Toarcian stage boundary is defined by the base of the *P. paltus* Zone, which is located ~15 m below the base of the sandstone-dominated interval in the Sakuraguchi-dani section (Fig. 3, see also Fig. 8 in Nakada and Matsuoka, 2011). The samples were analysed for bulk $\delta^{13}C_{org}$ and total organic carbon (TOC) values. Small pieces of rock sample were powdered using a stainless steel mortar. Powdered samples were decalcified in 6N HCl, and then washed in purified water until neutrality was reached. Dried samples were weighed into Sn foil cups and analysed on a FLASH2000 (Thermo Finnigan) elemental analyzer linked to a DELTAplus Advantage (Thermo Finnigan) isotope ratio mass spectrometer, housed at Geo-Science Laboratory (Chikyu Kagaku Kenkyusho), Nagoya, Japan. Glycine (SI Science Reference Material, Lot No.: M2M9103, $\delta^{13}C_{org}$ = – 31.9 ‰), L-Alanine (SI Science Reference Material, Lot No.: SS16, $\delta^{13}C_{org}$ = – 19.7 ‰), and L-Histidine (SI Science Reference Material, Lot No.:

M5P8062, $\delta^{13}C_{org}$ = – 10.6 ‰) were used as working standards. Analytical precision was ± 0.1 ‰ determined by repeat measurements of the working standards.

*3.2. Analysis of pyrite framboids: background and analytical procedure*

To reconstruct palaeo-ocean redox conditions (Tyson and Pearson, 1991; Table 1), 5 silty mudstone samples were analysed for the size distribution of pyrite framboids. For framboid size-distribution measurements, silty mudstone samples were cut perpendicular to the bedding planes and polished into thin sections. These thin sections were observed using a scanning electron microscope (SEM) (JSM-6010LA, JEOL, Japan) housed at Kokushikan University, Tokyo, Japan. The SEM was set in backscatter mode, which allows the mineralogy and the fabric to be readily evaluated. The pyrite framboid size population for each silty mudstone thin section was evaluated by measuring up to 100 separate framboids. Size-frequency distributions are described here via calculation of the mean, standard deviation, minimum, maximum, first quartile, and third quartile (Fig. 3). The obtained framboid size data were statistically evaluated to test for statistically significant changes in size populations between samples. As the pyrite framboid size populations were not normally distributed (see Section 4.2 and Fig. 3), we used a Steel-Dwass test, a nonparametric multiple comparison procedure, to statistically compare size populations.

*3.3. Analysis of available redox-sensitive trace element data*

In addition to pyrite framboid analysis, additional geochemical proxies were evaluated to further constrain redox conditions that prevailed during the deposition of mudstones in the Nishinakayama Formation. Specifically, redox-sensitive trace element (RSTE) data, previously reported in a separate study (Kemp and Izumi, 2014), were utilised. The V and Mo data from Kemp and Izumi (2014) were analysed because these are RSTEs that have "strong euxinic affinity" (as defined in Algeo and Maynard, 2004).

RSTEs of strong euxinic affinity are elements that are taken up in solid solution by Fe-sulfide or involved in other reactions catalysed by free $H_2S$, and that are resident mainly in authigenic phases (Algeo and Maynard, 2004). Based on such characteristics, the concentration pattern of RSTEs of strong euxinic affinity in marine mudstones is considered to represent different responses to bottom-water redox conditions (Algeo and Maynard, 2004). In particular, it is possible that benthic redox conditions can be distinguished by using a simple cross-plot diagram showing the relationship between Al-normalized RSTEs of strong euxinic affinity and TOC (Algeo and Maynard, 2004; Tribovillard et al., 2006). In this study, V/Al and Mo/Al values of mudstones from the Nishinakayama Formation were calculated by using the dataset of the previous study (appendix A in Kemp and Izumi, 2014). RSTE data in the Nishinakayama Formation mudstones was obtained from –17.02 m (~Pliensbachian/Toarcian boundary) to 53 m (lower Toarcian) from the Sakuraguchi-dani section. The RSTE and Al data used were measured on a Thermo ICAP 6300 ICP-AES (see Kemp and Izumi, 2014 for full analytical procedure). Using these data, we calculated the element enrichment factors ($X_{EF}$; Tribovillard et al., 2006), in which sample concentrations are normalised to the average value of upper continental crust (AUCC, McLennan, 2001), as calculated following the formula below:

$$X_{EF} = (X_{sample}/Al_{sample})/(X_{AUCC}/Al_{AUCC}), \quad (1)$$

where X is the weight concentrations of the RSTE under consideration. Based on this normalised enrichment factor, we can assess how many times larger (or smaller) the detected elemental concentration is compared to average crustal material before erosion and sedimentation.For this study, AUCC values for Al (8.04 wt.%), V (107 ppm), and Mo (1.5 ppm) are from McLennan (2001).

## 4. Results

### *4.1 New carbon-isotope and TOC data from the upper Pliensbachian*

Results of our new $\delta^{13}C_{org}$ and TOC analyses are shown in Table 2 and Figure 3. TOC values from the new upper Pliensbachian outcrop (from ~–27 to ~–22 m) range from 0.96 to 1.69 wt.% with a mean value of 1.27 wt.% (Fig. 3). Combined with previously reported TOC data from Kemp and Izumi (2014), TOC contents slightly increase from the upper Pliensbachian in to the early Toarcian (Fig. 3). During the T-OAE interval (characterized by the $\delta^{13}C_{org}$ negative excursion), TOC contents show generally higher values (Fig. 3).

The $\delta^{13}C_{org}$ values from the new outcrop range from –23.6 to –24.6 ‰ (Fig. 3). Although the upper Pliensbachian $\delta^{13}C_{org}$ values show little variation, it is notable that prior to the T-OAE interval a gradual fall in $\delta^{13}C_{org}$ can be recognized from the upper Pliensbachian to early Toarcian (from ~–27 to ~–5 m; Fig. 3). In a number of European successions, the stage boundary between the Pliensbachian and Toarcian is characterized by a short-term $\delta^{13}C_{org}$ negative excursion of up to ~2 ‰ (e.g. Littler et al., 2009; Suan et al., 2008). A recent study has suggested that this Pliensbachian-

Toarcian boundary excursion may not have a global expression (Bodin et al., 2016). Similarly, an excursion is not recognized in our Sakuraguchi-dani data, although it is possible that one exists within the interval from ~–22 to ~–17 m with no outcrop (Fig. 3). A negative shift in $\delta^{13}C_{org}$ is present at ~15 m (Kemp and Izumi, 2014; Fig. 3), but this feature is defined by a single datapoint (Fig. 3).

*4.2 Pyrite petrology and size distribution of pyrite framboids*

Our SEM observations reveal distinct changes in petrology and framboid size distribution throughout the studied succession (Figs. 3 and 4). Framboids were present in all analysed mudstone samples (Fig. 4), and amorphous pyrite lumps were also present in all samples but were less common in the samples 2015-5-3.30 (–0.7 m height) and 2010-8-2.5 (10.4 m height) relative to the other samples. Key results from our pyrite framboid size analysis are summarized in Table 3. Small-sized framboids are especially rich in the samples 2015-5-3.30 (–0.7 m height) and 2010-8-2.5 (10.4 m height). Our statistical analysis shows that the mean framboid diameter of each of these samples is 4.4 μm, with a standard deviation (SD) of 1.8 μm (Fig. 3). In contrast, large-sized (>10 μm) framboids are more common in samples 2016-3B-0.50 (–23.3 m height), 2010-12-2 (21.9 m height), and 2010-16-5 (48 m height), and these samples have larger mean and standard deviation values (Fig. 3). Statistical analysis (Steel-Dwass test) of the size data indicates that the pyrite framboid sizes are significantly ($p < 0.01$) different between samples 2016-3B-0.50 (–23.3 m height) and 2015-5-3.30 (–0.7 m height), 2010-8.25 (10.4 m height) and 2010-12-2 (21.9 m height), 2010-12-2 (21.9 m height) and 2010-16-5 (48 m height), whereas there is no significant ($p > 0.05$) difference between the samples 2015-5-3.30 (–0.7 m height) and 2010-8-2.5 (10.4 m height) (see Fig. 3).

Framboid size populations that have been used to interpret palaeo-ocean redox conditions in previous studies show mostly unimodal distributions (e.g. Wignall et al., 2010; Li et al., 2016). Histograms of pyrite framboid sizes in this study also show unimodal distributions (Fig. 3). Figure 5 shows the relationship between mean framboid diameter and SD. According to this diagram, mudstones of –0.7 m height (main phase of the $\delta^{13}C_{org}$ excursion; Fig. 3) and of 10.4 m height (main phase/recovery phase transition; Fig. 3) were deposited under euxinic conditions (Wilkin et al., 1996; Wignall and Newton, 1998; Bond et al., 2004). In contrast, framboid data from the other three mudstone samples plot in the area indicative of “oxic-dysoxic” conditions (Fig. 5).

*4.3 Redox-sensitive trace element data*

Figure 6 summarizes the results of our geochemical data analysis. Following Algeo and Maynard (2004), Al-normalized V and Mo data are plotted against TOC as cross-plot diagrams (Fig. 6; see also Fig. 7 for a schematic illustration). Based on these cross-plots, most of the data plot in the area of the graph suggestive of oxic-suboxic depositional conditions, characterized by the absence of correlation between Al-normalized RSTE and TOC (Tribovillard et al., 2006; Fig. 6). In addition, because RSTEs in mudstones deposited under oxic-suboxic condition are considered to have been mainly supplied via detrital input (Tribovillard et al., 2006), there should be a strong positive correlation between terrigenous element proxies (e.g. Al, Ti) and RSTE concentrations. In the case of the Nishinakayama Formation mudstones, V abundances are strongly correlated with Al contents (Fig. 6; see also Fig. 7 in Kemp and Izumi, 2014), further supporting the idea that oxic-suboxic benthic conditions prevailed during mudstone deposition. Mo concentrations, on the other hand, do not show any correlation with Al (Fig. 6).

In terms of the enrichment factors, $V_{EF}$ and $Mo_{EF}$ range from 0.92 to 1.62 and 0.09 to 3.50 through the succession, respectively. These values are much lower compared with those interpreted to be from anoxic to euxinic environments. For instance, $Mo_{EF}$ from typical strongly anoxic to euxinic oceans such as the Black Sea and Cariaco Basin exceeds 100 or even 1000 due to high $H_2S$ (as reviewed by Algeo and Tribovillard, 2009). Similarly, $Mo_{EF}$ values reaching such high values in Toarcian sediments and within other geological periods have also been interpreted as evidence for euxinic conditions (Algeo and Maynard, 2004; Takahashi et al., 2014; Fujisaki et al., 2016).

## 5. Discussion

### *5.1 Redox history from the latest Pliensbachian to early Toarcian*

The mudstone geochemical cross-plots from the Nishinakayama Formation are suggestive of oxic-suboxic conditions (Fig. 6). This redox interpretation is also supported by enrichment factors of V ($V_{EF}$ = 0.92 to 1.62) and Mo ($Mo_{EF}$ = 0.09 to 3.50), which are lower than would be expected in typical anoxic to euxinic environments. Additionally, mudstone lithofacies analysis indicates that bioturbated/burrowed mudstones are also recognized intermittently throughout the studied succession (Izumi et al., 2012; Izumi et al., 2018; Fig. 2). This evidence suggests that dysoxic and/or suboxic bottom-water conditions were disrupted by at least intermittent short-term oxic conditions, supporting the observations and inferences of previous studies (Tanabe et al., 1991; Izumi et al., 2012; Kemp and Izumi, 2014).

To investigate things in more detail, RSTE data from the early Toarcian Nishinakayama Formation were compared to data from the early Toarcian Posidonia Shale of the Rietheim succession, Swiss Jura Mountains, northern Switzerland (Montero-Serrano et al., 2015; Fig. 7). This comparison was made because the litho- and biofacies of the Nishinakayama Formation have marked similarities with the Posidonia Shale succession (Tanabe et al., 1991). In addition, because redox conditions during deposition of the Posidonia Shale of the Rietheim succession have been reconstructed by Montero-Serrano et al. (2015) based on multi-proxy analysis (i.e. pyrite content, sulphide and organic balances, V/(V + Ni) ratios, RSTE enrichment factors, relationships between Al-normalized RSTE and TOC, and TOC/$P_{total}$ molar ratios), data comparison should provide useful insights in to redox interpretations of the Nishinakayama Formation. According to the cross-plot diagrams between Al-normalized V and TOC, and between V and Al (Fig. 7), data from the Nishinakayama Formation are very similar to that from the *semicelatum* Subzone of the Swiss Rietheim section – immediately prior to the $\delta^{13}C_{org}$ excursion (Etter, 1994; Montero-Serrano et al., 2015). These similarities are: 1) absence of correlation between V/Al and TOC (Fig. 7) and 2) a strong positive correlation ($r^2 > 0.8$) between V and Al abundances (Fig. 7). Based on the multi-proxy redox analysis by Montero-Serrano et al. (2015), they concluded that sedimentary deposition of the Rietheim Posidonia Shale succession during the *semicelatum* Subzone took place under oxic to dysoxic bottom-water conditions (Montero-Serrano et al., 2015). These lines of evidence are consistent with the idea that redox conditions during deposition of the Sakuraguchi-dani mudstones were dysoxic, with intermittent oxygenation.

In contrast to these RSTE data, however, framboid data from the mudstones at –0.7 m (main phase of the $\delta^{13}C_{org}$ excursion; Fig. 3) and 10.4 m (main phase/recovery phase of the excursion; Fig. 3) suggest that euxinic conditions occurred within the T-OAE interval in the Sakuraguchi-dani succession (Fig. 5). Framboid data have been suggested to represent a more robust redox proxy due to the suggested invariance of this proxy to diagenesis (Wilkin et al., 1997). Indeed, in the case of the Nishinakayama Formation, early diagenesis may have altered sediment geochemistry, as suggested by Tanabe et al. (1984). The precise temporal and spatial distributions of water-column euxinia, however, cannot be constrained by this study due to the lack of resolution. Nevertheless, the key point is that our framboid data provides, for the first time, evidence for at least intermittent water-column euxinia in a NW Panthalassic shallow-marine setting (Fig. 3; Table 3). Previous studies suggested that euxinia also occurred during the T-OAE in Tethyan shallow-marine settings and Panthalassic pelagic settings (e.g. Schouten et al., 2000; Bowden et al., 2006; van Breugel et al., 2006; Wignall et al., 2010; Fujisaki et al., 2016).

The mismatch between the RTSE data and the framboid data may be due to diagenetic influence on the sediment geochemistry (Tanabe et al., 1984; Wilkin et al., 1997). Equally, the mismatch could arise if oxygenation was variable throughout deposition of the Nishinakayama Formation. Indeed, the presence of bioturbated lithofacies in mudstone samples of 2015-5-3.30 (–0.7 m height; Table 3; Fig. 2D, E, see also Izumi et al., 2012) suggests dynamic, fluctuating redox conditions. This complexity and lack of constancy in redox conditions may not be surprising in a relatively shallow-water succession, and indeed similar findings have been made for

Toarcian OAE strata from Germany (Röhl et al., 2001). Alternatively, however, a more likely mechanism to explain the mismatch between the RSTE and framboid data is the development of an oxygen minimum zone (OMZ) in the water column during the main phase of the $\delta^{13}C_{org}$ excursion. Small pyrite framboids could form within this OMZ, which overlies otherwise oxygenated or perhaps suboxic bottom water. This mechanism has been used to explain low RSTE concentrations associated with small pyrite framboid sizes from Permo-Triassic sediments (Algeo et al., 2011; Takahashi et al., 2015).

*5.2 Potential cause of redox change during the T-OAE*

Our suggestion above that small framboids found within the T-OAE interval (–0.7 m and 10.4 m, Fig. 3) formed within a euxinic OMZ demands an explanation for why such an OMZ would form. Previous work has suggested that the T-OAE was characterised by enhanced hydrological cycling in Boreal, Tethyan, and Panthalassic locations (Cohen et al., 2004; Krencker et al., 2015; Brazier et al., 2016; Izumi et al., 2018). In the Sakuraguchi-dani section, recent geochemical and sedimentological analysis indicates a close association between the $\delta^{13}C$ excursion and evidence for high-energy advective sediment transport, enhanced fluvial discharge, and detrital input (Kemp and Izumi, 2014; Izumi et al., 2018; see also Fig. 3). We suggest that enhanced fluvial discharge and detrital input associated with a strengthening of the hydrological cycling during the $\delta^{13}C$ excursion elevated nutrient input to the sea, enhancing surface productivity. This enhanced primary productivity could have led to an expansion of an OMZ in the water column (Fig. 3; Table 3). Although the actual change in nutrient concentrations and palaeo-productivity at the NW Panthalassic shallow margin is unknown due to the absence of proxy data, this interpretation is in-line with that of Erba (2004) and Bodin et al. (2010), who drew similar conclusions based on work on Tethyan sections.

The occasional presence of advective sediment transport may explain the intermittent short-term benthic oxygenation events. In particular, sedimentary features indicative of high-energy advective sediment transport (i.e. sediment gravity flow deposits, ripples, fluid-mud deposits) are commonly recognized from the Nishinakayama Formation (Kawamura, 2010; Izumi et al., 2018; Fig. 3). Advective sediment transport could have helped oxygenate bottom waters via mixing, allowing intermittent faunal colonisation and hence bioturbation (Izumi et al., 2012, 2018; Fig. 2D, E).

## 6. Conclusions

To reconstruct the redox history of a NW Panthalassic shallow basin from the late Pliensbachian to early Toarcian, we employed geochemical and pyrite framboid analysis of the mudstone-dominated succession of the Nishinakayama Formation (Sakuraguchi-dani section, Toyora area, Japan). Results of our analysis suggest that oxic to suboxic (generally dysoxic) benthic conditions largely prevailed in our studied NW Panthalassic shallow-water environment. Framboid size-distribution analysis demonstrates that euxinic conditions occurred at least briefly during the main phase of the $\delta^{13}C$ negative excursion that characterizes the T-OAE. We suggest that this water-column euxinia was related to the expansion of an oxygen minimum zone caused by enhanced productivity. This interpretation is consistent with an inferred elevation of fluvial discharge and detrital input caused by a strengthening of the hydrological cycling concomitant with the OAE, as suggested by sedimentological analyses.

## Acknowledgments

Part of this work was financially supported by JSPS grants 15J08821 to KI. DBK acknowledges receipt of NERC Fellowship NE/I02089X/1, and grants from the Sasakawa Foundation of Great Britain and Daiwa Foundation. This study contributes to IGCP 655. We thank M. Ikeda, T. Ohta, K. Suzuki, S. Itamiya, and K. Kawano for assistance in the field and/or helpful discussion. Fieldwork was carried out with full permission and support from its landowners. Technical staff at Geo-Science Laboratory (Chikyu Kagaku Kenkyusho) are thanked for performance of TOC and carbon-isotope analysis.

## Appendix A. Supplementary data

Supplementary data to this article can be found online at http://dx.doi.org./xx.xxxx/j.palaeo.xxxx.xx.xxx.

## References

Algeo, T.J., Maynard, J.B., 2004. Trace-element behaviour and redox facies in core shales of Upper Pennsylvanian Kansas-type cyclothems. Chemical Geology 206, 289-318.

Algeo, T.J., Tribovillard, N., 2009. Environmental analysis of paleoceanographic systems based on molybdenum-uranium covariation. Chemical Geology 268, 211-225.

Algeo, T.J., Kuwahara, K., Sano, H., Bates, S., Lyons, T., Elswick, E., Hinnov, L., Ellwood, B., Moser, J., Maynard, J.B., 2011. Spatial variation in sediment fluxes, redox conditions, and productivity in the Permian-Triassic Phanthalassic Ocean. Palaeogeography, Palaeoclimatology, Palaeoecology 308, 65-83.

Al-Suwaidi, A.H., Angelozzi, G.N., Baudin, F., Damborenea, S.E., Hesselbo, S. P., Jenkyns, H.C., Mancenido, M.O., Riccardi, A.C., 2010. First record of the Early Toarcian Oceanic Anoxic Event from the Southern Hemisphere, Neuquén Basin, Argentina. Journal of the Geological Society, London 167, 633-636.

Bailey, T.R., Rosenthal, Y., McArthur, J.M., van de Schootbrugge, B., Thirlwall, M.F., 2003. Paleoceanographic changes of the Late Pliensbachian-early Toarcian interval: a possible link to the genesis of an Oceanic Anoxic Event, Earth and Planetary Science Letters 212, 307-320.

Bodin, S., Mattioli, E., Fröhlich, S., Marshall, J.D., Boutib, L., Lahsini, S., Redfern, J., 2010. Toarcian carbon isotope shifts and nutrient changes from the Northern margin of Gondowana (High Atlas, Morocco, Jurassic): palaeoenvironmental implications. Palaeogeography, Palaeoclimatology, Palaeoecology 297, 377-390.

Bodin, S., Krencker, F.-N., Kothe, T., Hoffmann, R., Mattioli, E., Heimhofer, U., Kabiri, L., 2016. Perturbation of the carbon cycle during the late Pliensbachian-early

Toarcian: New insight from high-resolution carbon isotope records in Morocco. Journal of African Earth Sciences 116, 89-104.

Bond, D.P.G., Wignall, P.B., Racki, G., 2004. Extent and duration of marine anoxia during the Frasnian-Famennian (Late Devonian) mass extinction in Poland, Germany, Austria and France. Geological Magazine 141, 173-193.

Bowden, S.A., Farrimond, P., Snape, C.E., Love, G.D., 2006. Compositional differences in biomarker constituents of the hydrocarbon, resin, asphaltene and kerogen fractions: an example from the Jet Rock (Yorkshire, UK). Organic Geochemistry 37, 369-383.

Brazier, J.-M., Suan, G., Tacali, T., Simon, L., Martin, J.E., Mattioli, E., Balter, V., 2015. Calcium isotope evidence for dramatic increase of continental weathering during the Toarcian oceanic anoxic event (Early Jurassic). Earth and Planetary Science Letters 411, 164-176.

Brunner, C.A., Beal, J.M., Bentley, S.Y., Furukawa, K., 2006. Hypoxia hotspots in the Mississippi Bight. Journal of Foraminiferal Research 36, 95-107.

Caruthers, A.H., Gröcke D.R., Smith, P.L., 2011. The significance of an Early Jurassic (Toarcian) carbon-isotope excursion in Haida Gwaii (Queen Charlotte Islands). British Columbia Canada. Earth and Planetary Science Letters 307, 19-26.

Caswell, B.A., Coe, A.L., 2013. Primary productivity controls on opportunistic bivalves during Early Jurassic ocean deoxygenation. Geology 41, 1163-1166.

Cohen, A.S., Coe, A.L., Kemp, D.B., 2007. The Late Paleocene-Early Eocene and Toarcian (Early Jurassic) carbon isotope excursions: a comparison of their time scales, associated environmental changes, causes and consequences. Journal of the Geological Society, London 164, 1093-1108.

Danise, S., Twichett, R.J., Little, C.T.S., Clemence, M-E., 2013. The Impact of Global Warming and Anoxia on Marine Benthic Community Dynamics: an Example from the Toarcian (Early Jurassic). Plos One, doi: 10.1371/journal.pone.0056255.

Dera, G, Pellenard, P., Niege, P., Deconinck, J-F., Puceat, E., Dommergues, J-L., 2009. Distribution of clay minerals in Early Jurassic peritethyan seas: palaeoclimatic significance inferred from multiproxy comparisions. Palaeogeography, palaeoclimatology, Palaeoecology 271, 39-51.

Erba, E., 2004. Calcareous nannofossils and Mesozoic oceanic anoxic events. Marine Micropaleontology 52, 85-106.

French, K.L., Sepúlveda, J., Trabucho-Alexandre, J., Gröcke, D.R., Summons, R.E., 2014. Organic geochemistry of the early Toarcian oceanic anoxic event in Hawsker Bottoms, Yorkshire, England. Earth and Planetary Science Letters 390, 116-127.

Fujisaki, W., Sawaki, Y., Yamamoto, S., Sato, T., Nishizawa, M., Windley, B.F., Maruyama, S., 2016. Tracking the redox history and nitrogen cycle in the pelagic Panthalassic deep ocean in the Middle Triassic to Early Jurassic: Insights from redox-sensitive elements and nitrogen isotopes. Palaeogeography, Palaeoclimatology, Palaeoecology 449, 397-420.

Gröcke, D.R., Hori, R.S., Trabucho-Alexandre, J., Kemp, D.B., Schwark, L., 2011. An open marine record of the Toarcian oceanic anoxic event. Solid Earth 2, 245-257, doi:10.5194/se-2-245-2011

Hesselbo, S.P., Gröcke, D.R., Jenkyns, H.C., Bjerrum, C.J., Farrimond, P., Morgans Bell, H.S., Green, O.R., 2000. Massive dissociation of gas hydrate during a Jurassic oceanic event. Nature 406, 392–395.

Hesselbo, S.P., Jenkyns, H.C., Duarte, L.V., Oliveira, L.C.V., 2007. Carbon-isotope record of the Early Jurassic (Toarcian) Oceanic Anoxic Event from fossil wood and marine carbonate (Lusitanian Basin, Portugal). Earth and Planetary Science Letters 253, 455–470.

Hirano, H., 1973. Biostratigraphic study of the Jurassic Toyora Group, part 3. Transactions and Proceedings of the Palaeontological Society of Japan, New Series 90, 45–71.

Huang, Y., Chen, Z.-Q., Wignall, P.B., Zhao, L., 2017. Latest Permian to Middle Triassic redox condition variations in ramp setting, South China: Pyrite framboid evidence. Geological Society of America Bulletin 129, 229-243.

Izumi, K., Miyaji, T., Tanabe, K., 2012. Early Toarcian (Early Jurassic) oceanic anoxic event recorded in the shelf deposits in the northwestern Panthalassa: Evidence from the Nishinakayama Formation in the Toyora area, west Japan. Palaeogeography, palaeoclimatology, Palaeoecology 315-316, 100-108.

Izumi, K., Kemp, D.B., Itamiya, S., Inui, M., 2018. Sedimentary evidence for enhanced hydrological cycling in response to rapid carbon release during the early Toarcian oceanic anoxic event. Earth and Planetary Science Letters 481, 162-170.

Jenkyns, H.C., 1988. The early Toarcian (Jurassic) anoxic event - stratigraphic, sedimentary, and geochemical evidence. American Journal of Science 288, 101-151.

Jenkyns, H.C., Gröcke, D.R., Hesselbo, S.P., 2001. Nitrogen isotope evidence for water mass denitrification during the early Toarcian (Jurassic) oceanic anoxic event. Palaeoceanography 16, 593-603.

Kafousia, N., Karakitsios, V., Jenkyns, H.C., Mattioli, E., 2011. A global event with a regional character: the Early Toarcian Oceanic Anoxic Event in the Pindos Ocean (northern Peloponnese, Greece). Geological Magazine 148, 619–631.

Kawamura, H., 2010. Stratigraphic revision of the Jurassic Toyora Group of the southern part of the Tabe Basin, Yamaguchi Prefecture, southwest Japan. Journal of the Geological Society of Japan 116(1), 27-44.

Kemp, D.B., Coe, A.L., Cohen, A.S., Schwark, L., 2005. Astronomical pacing of methane release in the Early Jurassic period. Nature 437, 396–399.

Kemp, D.B., Izumi, K., 2014. Multiproxy geochemical analysis of a Panthalassic margin record of the early Toarcian oceanic anoxic event (Toyora area, Japan). Palaeogeography, Palaeoclimatology, Palaeoecology 414, 332-341.

Kemp, D.B., Coe, A.L., Cohen, A.S., Weedon, G.P., 2011. Astronomical forcing and chronology of the early Toarcian (Early Jurassic) oceanic anoxic event in Yorkshire, UK. Paleoceanography 24, PA4210, doi:10.1029/2011PA002122.

Krencker, F.-N., Bodin, S., Suan, G., Heimhofer, U., Kabiri, L., Immenhauser, A., 2015. Toarcian extreme warmth led to tropical cyclone intensification. Earth and Planetary Science Letters 425, 120-130.

Lallier-Verges, E., Bertrand, P., Desprairies, A., 1993. Organic matter composition and sulfate reduction intensity in Oman Margin sediments. Marine Geology 112, 57-69.

Li, G., Wang, Y., Shi, G.R., Liao, W., Yu, L., 2016. Fluctuations of redox conditions across the Permian-Triassic boudary–New evidence from the GSSP section in Meishan of South China. Palaeogeography, Palaeoclimatology, Palaeoecology 448, 48-58.

Liao, W., Bond, D.P.G., Wang, Y., He, L., Yang, H., Weng, Z., Li, G., 2017. An extensive anoxic event in the Triassic of the South China Block: A pyrite framboid study from Dajiang and its implications for the cause(s) of oxygen depletion. Palaeogeography, Palaeoclimatology, Palaeoecology 486, 86-95.

McArthur, A.G., Algeo, T.J., van de Schootbrugge, B., Li, Q., Howarth, R.J., 2008. Basinal restriction, black shales, Re–Os dating, and the Early Toarcian (Jurassic) oceanic anoxic event. Paleoceanography 23, PA4217. doi:10.1029/2008PA001607.

McElwain, J.C., Wade-Murphy, J., Hesselbo, S.P., 2005. Changes in carbon dioxide during an oceanic anoxic event linked to intrusion into Gondwana coals. Nature 435 (7041), 479–482.

McLennan, S.M., 2001. Relationships between the trace element composition of sedimentary rocks and upper continental crust. Geochemistry, Geophysics, Geosystems 2(4).

Montero-Serrano, J.-C., Föllmi, K.B., Adatte, T., Spangenberg, J.E., Tribovillard, N., Fantasia, A., Suan, G., 2015. Continental weathering and redox conditions during the early Toarcian Oceanic Anoxic Event in the northwestern Tethys: Insight from the Posidonia Shale section in the Swiss Jura Mountains. Palaeogeography, Palaeoclimatology, Palaeoecology 429, 83-99.

Morten, S.D., Twitchett, R.J., 2009. Fluctuations in the body size of marine invertebrates through the Pliensbachian-Toarcian extinction event. Palaeogeography, Palaeoclimatology, Palaeoecology 284, 29-38.

Nakada, K., Matsuoka, A., 2011. International correlation of the Pliensbachian/Toarcian (Lower Jurassic) ammonoid biostratigraphy of the Nishinakayama Formation in the Toyora Group, southwest Japan. Newsletters on Stratigraphy 44, 89–111.

Neumann, T., Rausch, N., Leipe, T., Dellwig, O., Berner, Z., Bottcher, M.F., 2005. Intense pyrite formation under low sulfate conditions in the Achterwasser lagoon. SW Baltic Sea. Geochimica et Cosmochimica Acta 69, 3619-3630.

Page, K.N., 2003. The Lower Jurassic of Europe: its subdivision and correlation. Geological Survey of Denmark and Greenland Bulletin 1, 23–59.

Pearce, C.R., Cohen, A.S., Coe, A.L., Burton, K.W., 2008. Molybdenum isotope evidence for global ocean anoxia coupled with perturbations to the carbon cycle during the Early Jurassic. Geology 36, 231-234.

Percival, L.M.E., Cohen, A.S., Davies, M.K., Dickson, A.J., Hesselbo, S.P., Jenkyns, H.C., Leng, M.J., Mather, T.A., Storm, M.S., Xu, W., 2016. Osmium isotope evidence for two pulses of increased continental weathering linked to Early Jurassic volcanism and climate change. Geology 44, 759-762.

Röhl, H.J., Schmid- Röhl, A., Oschmann, W., Frimmel, A., Schwark, L., 2001. The Posidonia Shale (Lower Toarcian) of SW-Germany: an oxygen-depleted ecosystem controlled by sea level and palaeoclimate. Palaeogeography, Palaeoclimatology, Palaeoecology 165, 27-52.

Schallreuter, R., 1984. Framboidal pyrite in deep sea sediments. Initial Reports of the Deep Sea Drilling Project 75, 875-891.

Schmidt-Effing, R., 1972. Die Dactylioceratidae, eine Ammoniten-Familie des unteren Jura. Münstersche Forschungen zur Geologie und Paläontologie. 173 pp.

Schouten, S., van Kaam-Peters, H.M., Rijpstra, W.I.C., Schoell, M., Damste, J.S.S., 2000. Effects on an oceanic anoxic event on the stable carbon isotopic composition of early Toarcian carbon. American Journal of Science 300, 1-22.

Smith, A.G., Smith, D.G., Funnell, B.M., 1994. Atlas of Mesozoic and Cenozoic Coastlines. Cambridge University Press, Cambridge.

Suan, G., van de Schootbrugge, B., Adatte, T., Fiebig, J., Oschmann, W., 2015. Calibrating the magnitude of the Toarcian carbon cycle perturbation. Paleoceanography 30, 495-509.

Svensen, H., Planke, S., Chevallier, L., Malthe-Sorenssen, A., Corfu, F., Jamtveit, B., 2007. Hydrothermal venting of greenhouse gases triggering Early Jurassic global warming. Earth and Planetary Science Letters 256, 554–566.

Takahashi, S., Yamasaki, S., Ogawa, Y., Kimura, K., Kaiho, K., Yoshida, T., Tsuchiya, N., 2014. Bioessential element-depleted ocean following the euxinic maximum of the end-Permian mass extinction. Earth and Planetary Science Letters 393, 94-104.

Takahashi, S., Yamasaki, S., Ogawa, K., Kaiho, K., Tsuchiya, N., 2015. Redox conditions in the end-Early Triassic Panthalassa. Palaeogeography, Palaeoclimatology, Palaeoecology 432, 15-28.

Tanabe, K., 1991. Early Jurassic macrofauna of the oxygen-depleted epicontinental marine basin in the Toyora area, west Japan. Proceedings of Shallow Tethys (Saito Ho-on Kai Spec. Pub.) 3, 147-161.

Tanabe, K., Inazumi, A., Ohtsuka, Y., Katsuta, T., Tamahama, K., 1982. Litho- and biofacies and chemical composition of the Lower Jurassic Nishinakayama Formation (Toyora Group) in West Japan. Memoirs of Ehime University, Series D (Earth Science) 9, 47–62 (in Japanese with English abstract).

Tanabe, K., Inazumi, A., Tamahama, K., Takashi, K., 1984. Taphonomy of half and compressed ammonites from the lower Jurassic black shales of the Toyora area, west Japan. Palaeogeography, Palaeoclimatology, Palaeoecology 47, 329-346.

Trecalli, A., Spangenberg, J., Adatte, T., Follmi, K.B., Parente, M., 2012. Carbonate platform evidence of ocean acidification at the onset of the early Toarcian oceanic anoxic event. Earth and Planetary Science Letters 357-358, 214-225.

Tribovillard, N., Algeo, T.J., Lyons, T., Riboulleau, A., 2006. Trace metals as paleoredox and paleoproductivity proxies: An update. Chemical Geology 232, 12-32.

Tyson, R.V., Pearson, T.H., 1991. Modern and ancient continental shelf anoxia: an overview. In: Tyson, R.V., Pearson, T.H. (Eds.), Modern and Ancient Continental Shelf Anoxia. Geological Society, London, Special Publications 58, 1-26.

van Breugel, Y., Baas, M., Schouten, S., Mattioli, E., Sinninghe Damste, J.S., 2006. Isorenieratane record in black shales from the Paris Basin, France: Constraints on recycling of respired CO2 as a mechanism for negative carbon isotope shifts during the Toarcian oceanic anoxic event. Paleoceanography 21, PA4220, doi:10.1029/2006PA001305.

Von Hillebrandt, A., Schmidt-Effing, R., 1981. Ammoniten aus dem Toarcium (Jura) von Chile (Südamerika). Zitteliana 6, 3–74.

Wignall, P.B., Newton, R., 1998. Pyrite framboid diameter as a measure of oxygen deficiency in ancient mudrocks. American Journal of Science 298, 537-552.

Wignall, P.B., Bond, D.P.G., Kuwahara, K., Kakuwa, Y., Newton, R.J., Poulton, S.W., 2010. An 80 million year oceanic redox history from Permian to Jurassic pelagic sediments of the Mino-Tamba terrane, SW Japan, and the origin of four mass extinctions. Global and Planetary Change 71, 109-123.

Wilkin, R.T., Arthur, M.A., 2001. Variations in pyrite texture, sulfur isotope composition, and iron systematics in the Black Sea: evidence for late Pleistocene to Holocene excursions of the $O_2$-$H_2S$ redox transition. Geochimica et Cosmochimica Acta 65, 1399-1416.

Wilkin, R.T., Barnes, H.L., Brantley, S.L., 1996. The size distribution of framboidal pyrite in modern sediments: an indicator of redox conditions. Geochimica et Cosmochimica Acta 60, 3897-3912.

Wilkin, R.T., Barnes, H.L., Brantley, S.L., 1997. Formation processes of framboidal pyrite. Geochimica et Cosmochimica Acta 61, 323-339.

## Figure and Table captions

**Figure 1**. Palaeogeographic and geological settings of the study area (redrawn from Kemp and Izumi, 2014). (A) Early Jurassic Palaeogeographic map showing early Toarcian organic-rich deposits (modified from Jenkyns, 1988; Smith et al., 1994; Cohen et al., 2007). The map emphasizes the global nature of organic enrichment during the early Toarcian. (B) Inset map of Japan showing location of studied Sakuraguchi-dani succession (Yamaguchi prefecture). (C) Geological map of field area in the Tabe Basin (modified after Nakada and Matsuoka, 2011), with Sakuraguchi-dani route highlighted.

[1.5-column fitting image]

**Figure 2**. Selected photographs showing the studied field (Sakuraguchi-dani section) and distinct lithofacies of the mudstones. (A) Field photograph of approximately –3 to –2 m section height. Note the black-colored silty mudstones are dominant in the section. (B) Thin-section scan image and (C) photomicrograph of laminated silty mudstone. Sample ID: 2010-12-2 (height = 21.9 m). (D) Thin-section scan image and (E) photomicrograph of bioturbated dark mudstone. Note the completely homogeneous features, indicative of strong bioturbation. Sample ID: 2015-3-3.30 (height = –0.7 m).

[2-column fitting image]

**Figure 3**. Lithological log of the Sakuraguchi-dani section with carbon-isotope stratigraphy, TOC, and framboid data. Log is modified after Izumi et al. (2018), and biostratigraphical framework is based on Nakada and Matsuoka (2011). For carbon-isotope stratigraphy and TOC data, our new results (gray plots) are combined with data by previous works (Kemp and Izumi, 2014; Izumi et al., 2018). Framboid data are shown as box and whisker plots for each sample, with detailed size distribution histogram also shown (n = number of pyrite framboids measured for one sample; SD = standard deviation for diameter measurements). Framboid size differences between adjacent samples refer to results of Steel-Dwass statistical tests (see main text for details). Shaded intervals represent the main and recovery phases of carbon-isotope negative excursion characterizing the early Toarcian oceanic anoxic event (after Izumi et al., 2018). U. PLI. = Upper Pliensbachian.

[1-page fitting image]

**Figure 4**. Back scattered electron (BSE) images of pyrite framboids from the Sakuraguchi-dani section. (A) Magnified image of pyrite framboid from the sample 2016-3B-0.50 (–23.3 m). Scale bar = 10 μm. (B) An overview photograph showing the common presence of pyrite lumps, which sometimes occur as large clusters. Sample 2016-3B-0.50 (–23.3 m). Scale bar = 20 μm. (C) and (D) Overview photographs showing scattered distribution of small-sized pyrite framboids. Samples 2015-5-3.30 (–0.7 m) for Figure 4C, and 2010-8-2.5 (10.4 m) for Figure 4D, respectively. Scale bars = 10 μm. (E) Pyrite framboids with relatively large diameters from the sample 2010-12-2 (21.9 m). Scale bar = 20 μm. (F) Large-sized pyrite framboid from the sample 2010-16-5 (48 m). Scale bar = 10 μm.

[2-column fitting image]

**Figure 5**. Cross-plot of the mean diameter and standard deviation for analysed pyrite framboids from the Sakuraguchi-dani section. Dashed line is the threshold between euxinic and dysoxic–oxic conditions (after Wilkin et al., 1996; Bond et al., 2004).

[single column fitting image]

**Figure 6**. Key geochemical analysis results of the early Toarcian mudstone samples from the Sakuraguchi-dani section (data are from Kemp and Izumi, 2014). Redox-sensitive trace-elements (RSTEs) of strong euxinic affinity (cf. Algeo and Maynard, 2004) are analysed in this study to evaluate redox conditions. (Upper left) Cross-plot of TOC and Al-normalized V values of the Sakuraguchi-dani section, with anoxic and euxinic thresholds, as well as correlation lines of anoxic trends proposed by Algeo and Maynard, 2004. (Upper right) Cross-plots of Al, a representative terrigenous detrital proxy, and V. (Lower left) Cross-plot of TOC and Al-normalized Mo of the

Sakuraguchi-dani section. (Lower right) Cross-plots of Al and Mo. Most data plot in the “oxic-suboxic” area proposed by Tribovillard et al. (2006) (see also Fig. 7), suggesting that oxic to suboxic conditions prevailed during deposition of the Sakuraguchi-dani mudstones. In addition, under oxic-suboxic conditions, correlation of detrital proxy (Al) and RSTEs should be recognized because under these circumstances RSTEs are mainly associated with detrital flux (Tribovillard et al., 2006). This is verified by Figure 7 ($r^2 > 0.7$). See main text for details.

[2-column fitting image]

**Figure 7**. (Top figure) Theoretical model of the relationship between TOC and Al-normalized redox-sensitive trace-element (RSTE) of strong euxinic affinity, which can be useful to distinguish redox conditions (modified after Algeo and Maynard, 2004; Tribovillard et al., 2006). (Middle figure) Relationship between TOC and Al-normalized V, which is one of the key RSTEs of strong euxinic affinity (cf. Algeo and Maynard, 2004), of the lower Toarcian mudstone samples from the Nishinakayama Formation (Sakuraguchi-dani, Toyora area, Japan; Data from Kemp and Izumi, 2014) and Posidonia Shale (Rietheim, Swiss Jura Mountains, Switzerland; Data from Montero-Serrano et al., 2015). Swiss sec. = Swiss section, Sz. = Subzone. (Bottom figure) Cross-plot of Al and V values. Note that the plotted data of the Posidonia Shale from the Rietheim section were subdivided by ammonite Subzone. Solid regression lines show strong ($r^2 > 0.7$) correlations, and dashed regression lines show weak to moderate ($r^2 < 0.7$) correlations. Based on Figure 6, dysoxic conditions prevailed during deposition of the Sakuraguchi-dani mudstones and the Posidonia Shale *semicelatum* Subzone. See main text for details.

[1.5-column fitting image]

**Table 1**. Summary of criteria to distinguish redox conditions, based on lithofacies and pyrite framboid petrography.

**Table 2**. Results of carbon-isotope and TOC analysis.

**Table 3**. Summary of lithofacies observation and framboid measurements, with interpretations of redox conditions.

**Appendix A**. Spreadsheet for individual data of framboid size analysis, with statistic analysis results.

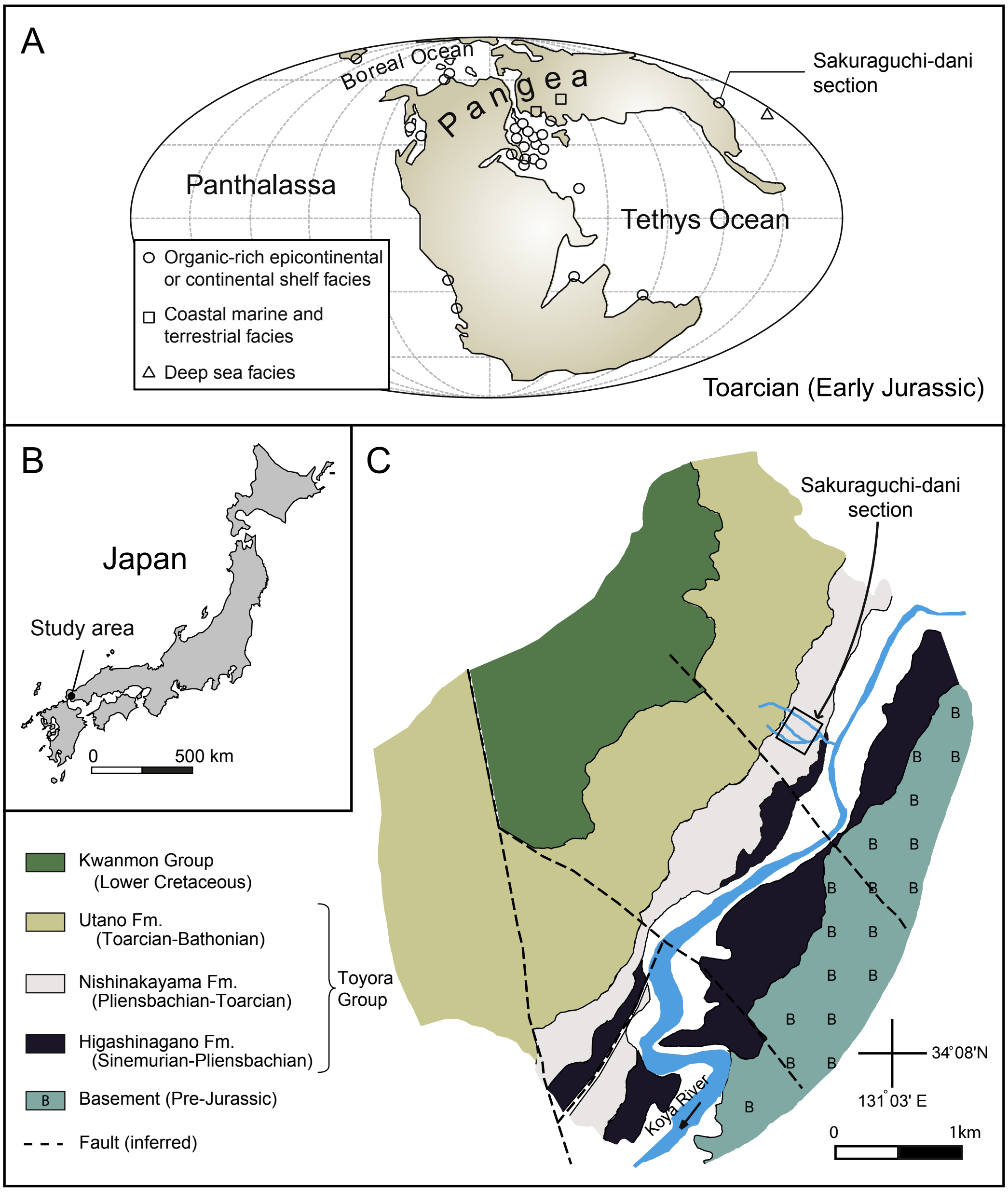


Izumi et al. (2017) - Figure 1

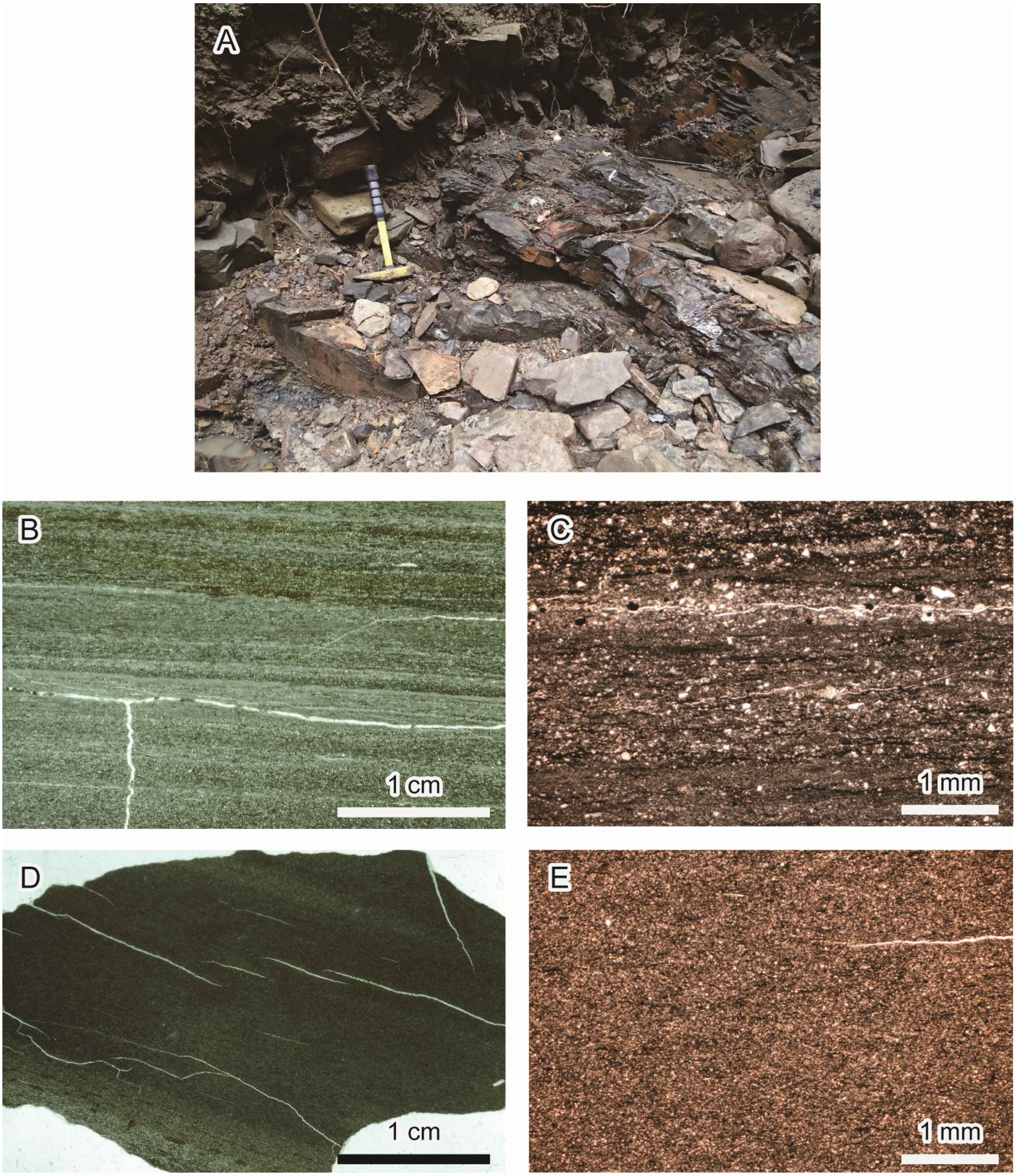


Izumi et al. (2017) - Figure 2

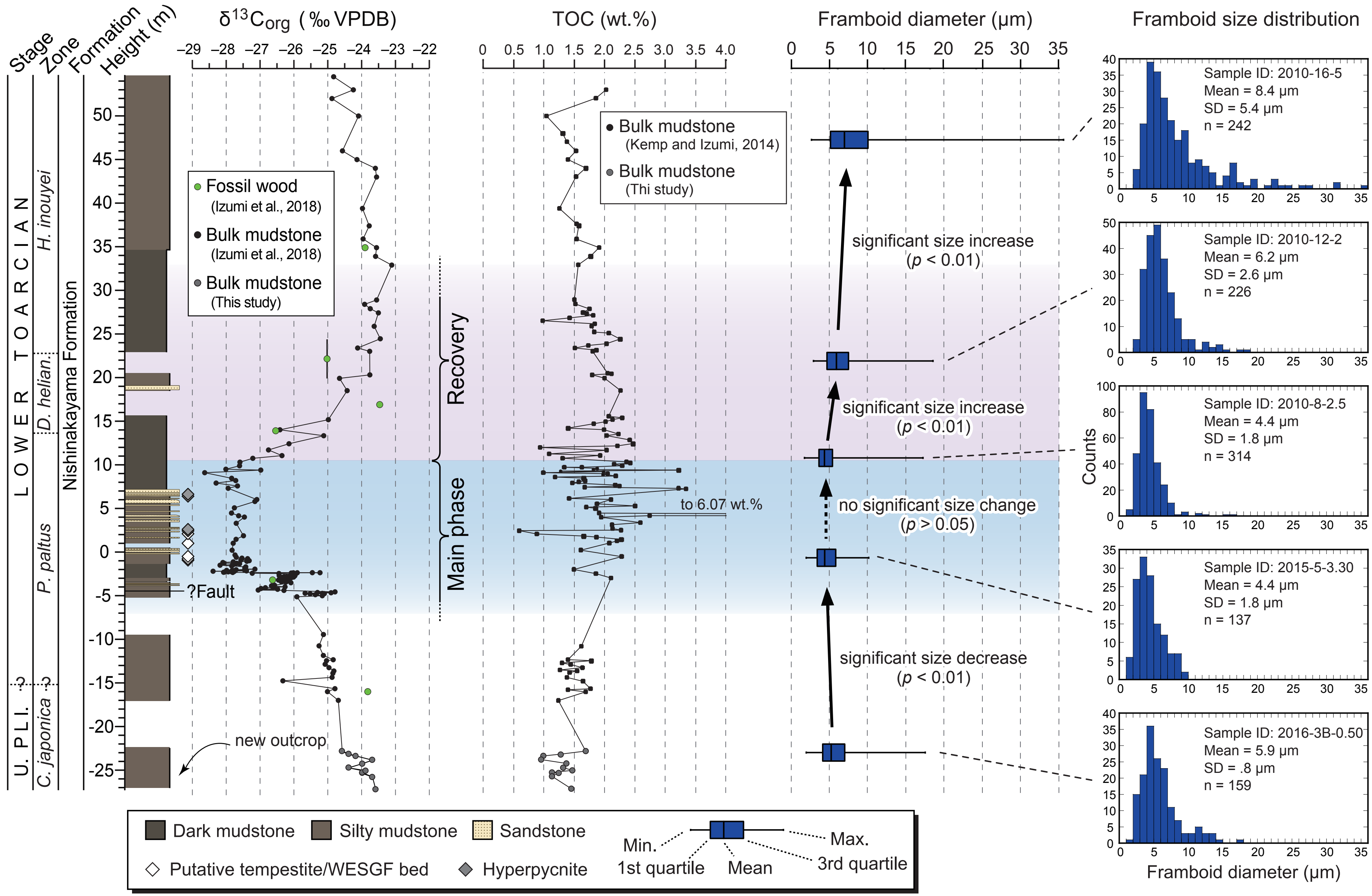


Izumi et al. (2017) - Figure 3

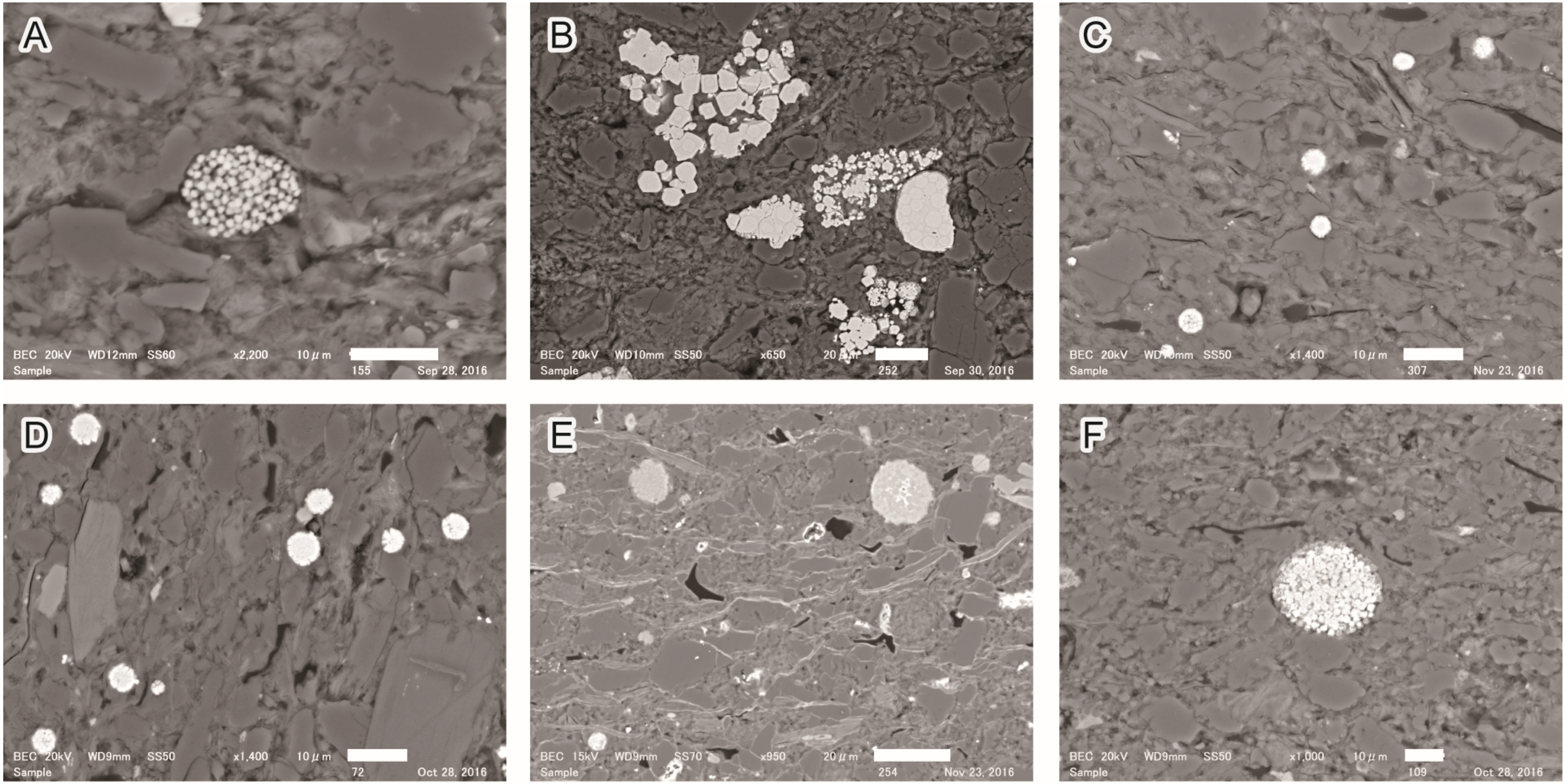


Izumi et al. (2017) - Figure 4

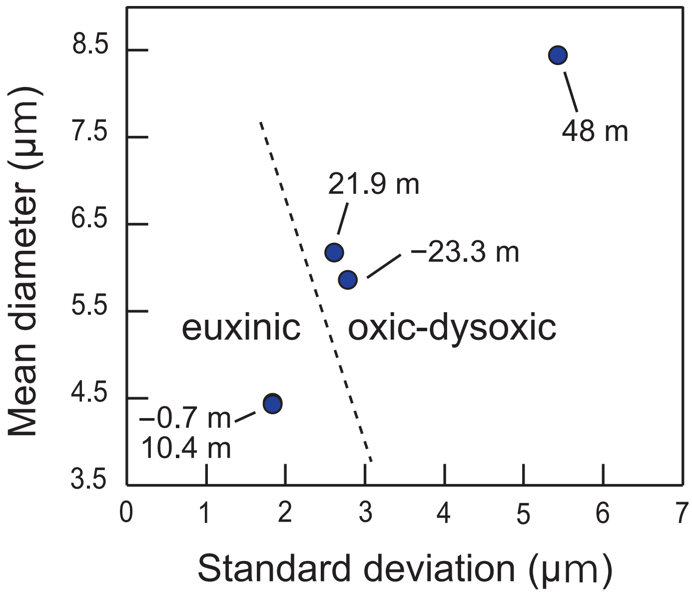


Izumi et al. (2017) - Figure 5

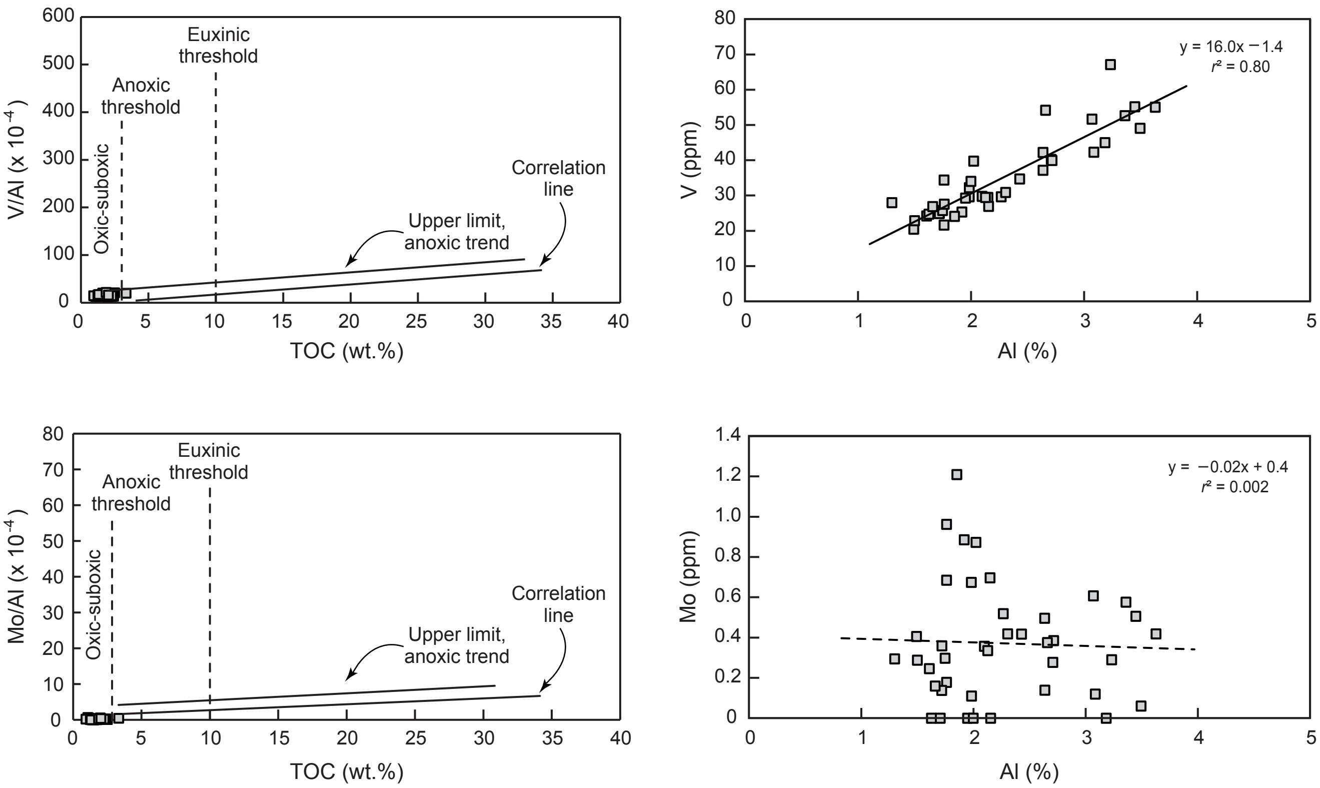


Izumi et al. (2017) - Figure 6

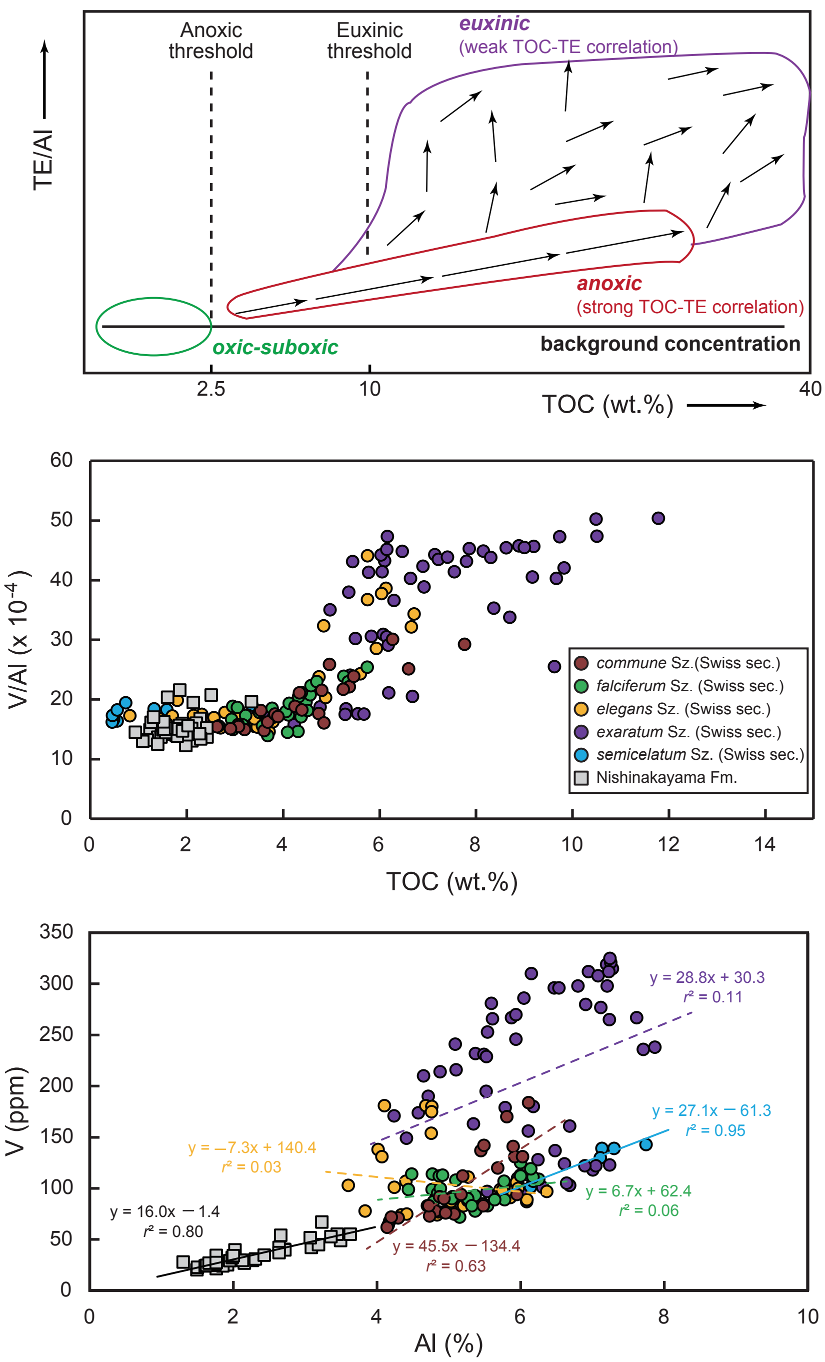


Izumi et al. (2017) - Figure 7